Macrophages display spatiotemporal specificity in intrahepatic cholangiocarcinoma and drive tumour progression via OSM and THBS1

Short title: Spatiotemporal macrophage profile in ICC progression

Tingjie Wang[1,3*], Ruitao Long[2*], Zhongyu Cheng[2], Mi Zhang[2], Bing Wei[1,3], Cong Lyu[1,3], Cuiyun Zhang[1,3], Guangbo Tang[4], Zihang Li[5], Lei,Li[2], Yida Li[6], Xiaofei Zhu[7], Chao Shi[1,3], Ke Yang[1,3], Chuanrui Xu[2#]

*Tingjie Wang and Ruitao Long contributed equally to this work.

[1]Department of Molecular Pathology, The Affiliated Cancer Hospital of Zhengzhou University, Henan Cancer Hospital, Zhengzhou, Henan, People's Republic of China.

[2]School of Pharmacy, Tongji Medical College, Huazhong University of Science and Technology, Wuhan, China

[3]Henan Key Laboratory of Molecular Pathology, Zhengzhou, People's Republic of China.

[4]Department of Clinical Medicine Research Center, The First Affiliated Hospital of Gannan Medical University, Ganzhou, Jiangxi, People's Republic of China.

[5]Department of Hematology, The First Affiliated Hospital of Xi'an Jiaotong University, No.277 Yanta West Road, Xi'an, Shaanxi, 710061, China.

[6]Department of Chemistry & Loker Hydrocarbon Research Institute, University of Southern California, Los Angeles, California 90089, United States.

[7]Henan Key Laboratory of Immunology and Targeted Drugs, Xinxiang Key Laboratory of Tumor Microenvironment and Immunotherapy, School of Medical Technology, Xinxiang Medical University, Xinxiang, People's Republic of China.

Corresponding author: Chuanrui Xu, School of Pharmacy, Tongji Medical College, Huazhong University of Science and Technology, Wuhan, Hubei, China. Email: xcr@hust.edu.cn

Keywords:

Intrahepatic cholangiocarcinoma, Spatiotemporal omics，Macrophage，OSM，THBS1

Electronic word count: 6769.

Number of figures and tables: 7.

Conflict of interest:

The authors declare no conflicts of interest to this work.

Financial support:

The research was supported by grants from National Natural Science Foundation of China (82472988, 82403200, 82372667, 82273059 and 82573814), Henan Province and Ministry of Health of Medical Science and Technology Program (SBGJ202302028 for T.W. and SBGJ202402032 for C.L.), Henan Province Science and Technology Research Project (242102310051), and Henan Province Clinical Research-Oriented Physician Training Program (HNCRD202413).

Authors contributions:

C.X., T.W. designed the study. T.W., C.Z., analyzed the multi-omics data. R.L. performed experiments. T.W., R.L. wrote the manuscript. C.X. revised the article. Z.C, M.Z., C.L., B.W., L.L., X.Z. handled sample preparation. Y.L., G.T., C.S., K.Y., Z.L. managed data collection, organization. All authors read and approved the manuscript.

Data availability:

The scRNA-seq data generated in this study are available from the GEO database under accession code GSE308574. The remaining data are available within the manuscript, supplementary information, or from the corresponding author upon reasonable request.

ABSTRACT

Background & Aims: Tumour-associated macrophages (TAMs) are abundantly found in intrahepatic cholangiocarcinoma (ICC) and are associated with poor prognosis, yet their spatiotemporal dynamics and role in ICC progression remain unclear. This study aimed to elucidate the transcriptional regulation heterogeneity of TAMs and uncover their interactions with ICC cells in driving tumour malignancy beyond immune suppression.

Methods: Using a time-resolved AKT1/NICD1 ICC model and patient datasets, we mapped the spatiotemporal macrophage landscape and their role in tumour progression. By integrating cell-cell communication analysis with phosphoproteomics, we validated key signalling cascades using TAM-ICC co-culture, multiplex immunofluorescence, gene silencing, and conditional knockout mouse models. Single-cell ATAC-seq further revealed epigenomic profiles of TAM subsets and identified their regulatory networks.

Results: Immune response Mφ_CXCL9 and inflammatory Mφ_S100A were enriched in early ICC lesions, while in advanced tumours an M2-like subset— Mφ_VEGFA— with high *VEGFA, ARG1, GPNMB, SPP1*, and *C1QA*, emerged as the major population and correlated with poor prognosis. Spatial transcriptomics revealed abundant Mφ_VEGFA infiltration at tumour boundaries with secretory and proliferative signatures. Further, Mφ_VEGFA drove tumour cell proliferation via the OSM-OSMR-STAT3-CCND1 axis and promoted invasion through THBS1-CD47-mTOR-DNB1 signalling. Lastly, MAFB directed M2 polarisation and upregulated *OSM/THBS1* in Mφ_VEGFA.

Conclusions: Mφ_VEGFA TAMs accumulate at the tumour boundary in late-stage ICC, driving proliferation and invasion via *OSM* and *THBS1* signalling, underscoring the potential of macrophage-targeted therapy in ICC.

Impact and implications

Our integrative spatiotemporal single-cell and spatial analyses define functionally distinct TAM subsets in ICC and identify a boundary-enriched Mφ_VEGFA population with Mafb-driven M2 programs that promotes tumour growth and invasion via OSM-OSMR and THBS1-CD47 signalling, supporting macrophage-directed combination therapy, as dual blockade showed synergistic anti-tumour activity. These findings are relevant to hepatobiliary oncologists, immunologists, translational researchers, and patients, since boundary Mφ_VEGFA prevalence correlates with poor outcomes and serves as a biomarker for risk stratification. Clinically, physicians can apply TAM signatures (e.g., CD68, VEGFA, OSM/OSMR, THBS1/CD47) to guide patient selection and trial design, while researchers explore macrophage reprogramming and policymakers prioritise biomarker-driven combinations. Our conclusions stem from single-cell/spatial profiling analyses with preclinical validation; prospective multi-centre studies are required to confirm efficacy, safety, and generalisability across stages and populations.

Introduction

Intrahepatic cholangiocarcinoma (ICC), originating from the intrahepatic bile duct epithelium, shows rising global incidence. Its subtle early symptoms, aggressive nature, and chemotherapy resistance drive a 5-year survival rate below 10%.[1]

Targeted therapies and immune checkpoint inhibitors benefit some solid tumours, but responses in ICC remain inconsistent owing to its complex tumour microenvironment (TME).[2] Tumour-associated macrophages (TAMs), the most abundant immune cells in the ICC TME, promote immune suppression, angiogenesis, and stromal remodelling,[2, 3] fuelling progression and metastasis. Current TAM-targeting strategies—depletion, reprogramming, recruitment control, and functional regulation—show variable efficacy.[4, 5] Heterogeneity is a major barrier: $CD163^+$ macrophages have low CSF-1R, reducing CSF-1R inhibitor response; CCL2 inhibitors are of limited use as CCR2 is also expressed on T and NK cells; and prolonged macrophage depletion disrupts immune homeostasis, causing adverse effects.[4] Thus, dissecting communication cascades between ICC cells and TAMS is critical to identify therapeutic targets that directly modulate ICC.

Distinct TAM phenotypes are associated with ICC progression. $MARCO^+$ TAMs correlate with epithelial mesenchymal transition (EMT), angiogenesis, and hypoxia.[6] *S100P* and *SPP1*—markers distinguishing perihilar and peripheral cholangiocarcinoma—show differential macrophage infiltration tied to prognosis and grade.[7] Moreover, TAM states are highly dynamic. Prior multi-omics studies largely used patient samples, failing to track temporal polarisation across tumour stages.

Epigenetic regulation is also critically involved, but a temporal atlas of macrophage epigenetics in ICC is lacking.

Spatial distribution further influences TAM functions.[8] Spatial-omics have highlighted TAM heterogeneity.[9, 10] TAMs at invasive fronts mainly express pro-angiogenic factors such as VEGFA, while core TAMs activate immunosuppressive pathways.[6] Moreover, TAM plasticity is shaped by cues such as extracellular matrix (ECM) gradients, lactate accumulation, and cytokines.[9] However, the spatial dynamics of TAMs in ICC remain poorly defined.

Here, we developed a temporal ICC mouse model, tracked TAM evolution, and identified shared human subpopulations, mapping their transcriptional and regulatory landscapes. Using cell-cell communication analysis, co-culture, multiplex immunofluorescence, and knockout models, we validated key TAM factors in ICC progression. These findings are expected to support macrophage-targeted immunotherapy for ICC.

Materials and methods

Materials and methods for sample preparation, bioinformatic analysis, and experimental procedures are described in supplementary file.

Results

Mφ_VEGFA is dominant at the ICC boundary and linked to poor prognosis

To dissect macrophage subsets driving ICC malignancy, we established an AKT1/NICD1 induced ICC mouse model via hydrodynamic tail vein injection and collected liver tissue at day 7 (early ICC), day 15 (mid ICC), day 25 (mid/advanced ICC), and day 31 (advanced ICC). Single cell RNA sequencing (scRNAseq) was performed at all stages and spatial transcriptomics sequencing (spRNAseq) was performed at day 31, with integrated analysis of public human datasets (Table S1, Fig. S1A-F).

Four conserved TAM subsets were identified in mouse and human ICC: Mφ_CXCL9(human)/Mφ_Cxcl9(mouse),Mφ_S100A/Mφ_S100a,Mφ_C1QA/Mφ_C1qa, and Mφ_VEGFA/Mφ_Vegfa (Fig. 1A-B, S1，Table S2). Mφ_Cxcl9 and Mφ_S100a dominated early/mid-stage mouse ICC (Fig. 1B), while in humans, Mφ_CXCL9 localised to adjacent liver and elevated expression of *CXCL9*, *CXCL11*, and *CCL5* (Fig. S1C, S1G), while Mφ_S100A was enriched in human ICC tissues with elevated *CD68*, *VCAN*, *S100A4*, *S100A8* (Fig. 1C, S1C, S1G), suggesting an inflammatory early ICC microenvironment. In contrast, Mφ_C1QA/Mφ_C1qa and Mφ_VEGFA/Mφ_Vegfa were enriched in human ICC and advanced mouse ICC, with similar transcriptional signatures (Fig 1C). Mφ_VEGFA showed elevated *GPNMB*, *VEGFA*, *ARG1*, *APOE*, *TREM2*, and *SPP1* levels (Fig 1C，S1C, S1G), consistent with M2-like, tumour-promoting macrophages.[11, 12] Mφ_VEGFA showed significant enrichment in cytokine secretion and tumour proliferation pathways (Fig. S1H). Similar TAM subtypes and

temporal patterns were confirmed in AKT1/YAP1 ICC mice (Figure S2A–C). Kupffer cells (*Clec4f*$^{+}$*Mrc1*$^{+}$ *and Vegfa*/*Gpnmb*/*Spp1*-low), were abundant in AKT1/NICD1 and AKT1/YAP1 ICC tissues, likely from liver damage caused by hydrodynamic injection (Fig. 1C, S1G, S2A–D).

Analysis of dynamic macrophage temporal distribution using pseudo-time analysis showed that Mφ_Cxcl9 andMφ_S100a predominated the early pseudo-time branch, while Mφ_Vegfa progressively expanded in later branches (Fig 1D), indicating that Mφ_VEGFA is the dominant population in advanced ICC tissues. Prognostic analysis across three independent cohorts (GSE89749,[13] GSE107943,[14] GSE244807[15]) confirmed the robust association of Mφ_VEGFA with poor outcome of patients with ICC (Fig. 1E, S2E).

In mouse ICC allografts, established by co-injection of BMDMs with BR ICC cells, tumour growth was significantly enhanced by macrophages, characterised by F4/80^{+} and CD206^{+} (Fig. 1F-i, S3A-G), while depletion of macrophages using clodronate liposome (Fig. S4A-D) suppressed tumour progression (CD11b^{+}F4/80^{+}/CD45^{+}), evidenced by increased liver-to-body weight ratio (Fig. 1F-ii).

Using spatial transcriptomics of day 31 mouse tumours and public human ICC data,[16] we resolved non-malignant, boundary, and core regions and resolved their underlying cell compositions (Fig. 1G–H, S5A–C). The M_Vegfa/Mφ_VEGFA cluster was enriched at the tumour boundary, with *VEGFA*, *SPP1, CD206*, and *CD68* enrichment (Fig. 1G–H, S5A-C). IF and IHC in human ICC tissue microarrays and mouse tissues validated the presence of CD206^{+}/CD68^{+} macrophages adjacent to ICC

182 cells that were Ki-67^{+}/CK19^{+} (Fig. S5 D–E).

183 Co-culture of ICC cells with macrophages caused M2-like polarisation of
184 macrophages, with robust upregulation of M2 polarisation markers including *ARG1*,
185 *VEGFA*, *IL10*, and *MRC1* (Fig. S6A-F), using non-contact Transwell co-cultures or
186 treatment with tumour-conditioned medium (TCM)(Fig. S6B-D). In Transwell co-
187 culture systems, EdU incorporation assay and migration assay demonstrated that
188 macrophage co-culture significantly enhanced ICC cell proliferation (Fig. S7A-D) and
189 migration (Fig. S7E). Together, these findings indicate that M2-like Mφ_VEGFA
190 accumulate at the ICC boundary, driving proliferation and invasion through cytokine
191 secretion.

192

193 **Mφ_VEGFA promotes ICC proliferation via the *OSM-OSMR-STAT3-CCND1* axis**

194 To explore the mechanisms underlying Mφ_VEGFA-mediated ICC progression, we re-
195 clustered and obtained seven epithelial cell subpopulations from human and
196 AKT1/NICD1 mouse ICC. Within human/mouse shared subtypes, E_Alb in mice or
197 E_ALB in human were normal hepatic epithelial cells with high *ALB* levels (Fig. 2A,
198 2B, S8A). E_Fxyd2 (mouse) or E_FXYD2 (human) were normal cholangiocytes with
199 high *FXYD2* levels (Fig. 2A, 2B, S8A). In contrast, E_Jun/E_Spp1 (mouse) and
200 E_CD74/E_IGFBP7 (human) showed high CNV scores (Fig. S8B) and were identified
201 as ICC cells. Specifically, E_Jun (mouse)/E_Cd74 (human) displayed high expressions
202 of *STAT3*, *JUN*, *HSPA1A* and *CCND1* (Fig. 2A, S8A), indicating their stress-responsive
203 and highly proliferative nature.[17, 18] Meanwhile, E_Jun/E_Spp1 (mouse) and

204 E_IGFBP7 (human) exhibited high levels of the EMT-related genes *VIM, COL4A1*, and
205 *FN1* (Fig. 2A, S8A). In addition, E_Mki67 (mouse)/E_MKI67 (human) displayed high
206 expressions of MKI67 but low expressions of receptor genes.
207 Integration of three cell-cell communication approaches (CellChat, CellphoneDB,
208 NicheNet) to analyse interactions between Mφ_VEGFA and ICC cells with high
209 proliferation and EMT features and the downstream signalling pathways, revealed that
210 Mφ_Vegfa engages with ICC cells via *Osm* and *Thbs1* ligands (Fig. 2C–D). *OSM*,
211 enriched in Mφ_Vegfa (mouse) and Mφ_VEGFA (human), interacted with ICC cells of
212 E_Jun in mice and E_CD74 in human via *OSMR* and *LIFR*, which in turn activated the
213 genes involved in cytokine response and epithelial proliferation (Fig. 2E, S8C–D).
214 To test whether OSMR and LIFR are required for ICC progression, we generated *Osmr*-
215 or *Lifr*- liver conditional knockout mice Osmr$^{fl/fl}$;Alb-cre and Lifr$^{fl/fl}$;Alb-cre, followed
216 by hydrodynamic injection of AKT1/NICD1 via tail vein. Compared with Lifr $^{fl/fl}$ mice,
217 Lifr $^{fl/fl}$; Alb-Cre mice showed no significant difference in liver-to-body weight ratio
218 upon AKT1/NICD1 injection (Fig. 2F–G, S9A-B). However, Osmr $^{fl/fl}$;Alb-Cre mice
219 exhibited a marked reduction of liver-to-body weight ratio after AKT1/NICD1 injection
220 compared to Osmr $^{fl/fl}$ mice (Fig. 2F–G, S9A-B). qRT-PCR revealed that *Osm* and *Osmr*
221 levels increased with tumour progression (Fig. S9C). Spatial interaction analysis,
222 scRNAseq in ICC cohorts (GSE210066 and GSE201425, Table S1, Fig. S10), and
223 spatial mapping by multiplex IF confirmed the presence of OSM^{+} macrophages (CD68^{+})
224 in the vicinity of OSMR^{+} tumour cells (CK19^{+}) (Fig. 2H, S10).
225 Functionally, RAW264.7 and QBC939 co-cultures increased *OSM*, *VEGFA*, and

226 *IL10* in macrophages, and *OSMR* in QBC939 cells (Fig. 3A, S11A). Similarly, co-
227 culture with BMDMs increased OSMR protein levels in BR cells (Fig. S3B-i).
228 Recombinant OSM increased OSMR mRNA and protein levels, and viability of ICC
229 cells (Fig. 3B). OSMR knockdown (siRNA) significantly suppressed ICC cell viability
230 (Fig. S11C-D). Similarly, CRISPR-Cas9-mediated knockout of *OSMR* resulted in
231 significantly decreased proliferation, viability, and clonogenicity of ICC cells (Fig. 3C,
232 S11E).
233 Phosphoproteomics of QBC939 cells treated with recombinant OSM revealed
234 enrichment of PI3K-AKT, MAPK, and cell cycle-related pathways (Fig. 3D). Moreover,
235 *Osmr* in the tumour subtype E_Jun was involved in epithelial cell proliferation,
236 cytokine response, and MAPK pathways, and interacted with *Stat3* and *Ccnd1* (Fig.
237 3E). Thus, OSM-OSMR may activate STAT3-CCND1 signalling in tumour cells. To
238 test this hypothesis, we used $Osmr^{fl/fl}$;Alb-Cre mice injected with AKT1/NICD1. H&E
239 and IHC staining demonstrated that ICC lesions formed in $Osmr^{fl/fl}$;Alb-Cre mice were
240 significantly smaller than those in $Osmr^{fl/fl}$ mice (Fig. 3F, S12A). Notably, *Osmr*
241 knockout did not alter $F4/80^{+}$ and $CD206^{+}$ macrophage infiltration levels (Fig. S12B).
242 However, the levels of the downstream proteins CCND1, BCL2, and p-STAT3 were
243 markedly reduced (Fig. 3G), indicating that Mφ_VEGFA promotes ICC growth via
244 OSM-OSMR signalling and downstream STAT3 phosphorylation, suggesting that
245 deficiency of OSM-OSMR signalling leads to retarded ICC growth in mice.
246
247 **Mφ_VEGFA TAMs promote ICC invasion through the *THBS1-CD47-mTOR-***

248 ***DBN1* axis**

249 In addition to *OSM, THBS1* is secreted by Mφ_VEGFA which may promote ICC
250 development. Cell communication analysis showed that *THBS1* interacted with E_Jun
251 and E_Spp1 in AKT1/NICD mouse ICC tissues and with E_IGFBP7 in human ICC via
252 *CD47* (Fig. 4A, Fig. S13A). Using NicheNet, we found that *THBS1*-regulated target
253 genes in ICC cells were mainly enriched in EMT-related signalling (Fig. 4B, S13).
254 Subsequently, we validated the THBS1-CD47 interaction both in vitro and in vivo. In
255 vitro, recombinant THBS1 exhibited moderate growth-promoting and enhanced pro-
256 migratory effects in ICC cells (Fig. S14A, B). Specifically, treatment with 10 ng/mL
257 recombinant THBS1 significantly enhanced wound-healing (Fig. 4C) and migration of
258 ICC cells (Fig. 4D). Correspondingly, *CD47* silencing significantly impaired the
259 stimulatory effects of THBS1 in promoting ICC cell migration (Fig. 4E–F, Fig. S14C,
260 D). Stable knockdown of *Cd47* in BR cells significantly inhibited the proliferation,
261 colony formation capability and viability of ICC cells (Fig. 4G–J). Co-culture with
262 BMDMs promoted BR migration ability, whereas *Cd47* knockdown blocked this effect
263 (Fig. 4K). Similarly, *Cd47* silencing inhibited subcutaneous allograft growth in mice
264 (Fig. 4L, Fig. S14E, F). Moreover, *Cd47* knockdown markedly suppressed ICC
265 dissemination in a peritoneal metastasis mouse model, as evidenced by reduced
266 metastatic nodule formation and decreased ascites accumulation (Fig. 4M(i-ii), Fig.
267 S14G, H). Consistently, CD47 silencing attenuated ICC growth and local invasion into
268 the surrounding hepatic parenchyma in the primary ICC mouse model (Fig. 4M-iii).

269 To elucidate the role of *THBS1*-mediated EMT in ICC, we performed western

270 blotting, which revealed that recombinant THBS1 induced rapid induction of EMT-
271 related proteins at 10 min with a peak at 2 h, accompanied with increased levels of p-
272 mTORC1 and downstream p-RPS6 (Fig. 5A, S15A). Phosphoproteomic analysis of
273 HuCCT1 cells treated with recombinant THBS1 at 0, 2, and 12 h revealed elevated
274 phosphorylation of PI3K-AKT and EMT-related signalling proteins at 2 h (Fig. 5B). In
275 comparison, differential protein phosphorylation was enriched in cell adhesion and
276 RNA metabolism pathways at 12 h (Fig. 5B, S15B). Specifically, ranking differentially
277 phosphorylated sites by fold change (2 h vs 0 h) identified DBN1 Ser142 as the most
278 strongly upregulated phosphorylation site at 2 h (Fig. 5C).

279 Co-culture of ICC cells with BMDM led to increased *Arg1, Vegfa*, and *Thbs1* in
280 BMDMs, CD47, p-mTORC1, p-DBN1 and Vimentin in ICC cell lines (Fig. 5D, Fig.
281 S16A–B). The upregulation of *Thbs1* and *Cd47* was also detected by qRT-PCR in
282 AKT1/NICD1-induced liver tissues (Fig. S16C–D). Inhibition of mTORC1 by
283 rapamycin substantially suppressed the pro-migratory effect of BMDMs on ICC cells
284 (Fig. 5E) and completely abrogated the THBS1-induced migration (Fig. 5F), indicating
285 that THBS1 promotes ICC cell migration via mTORC1 activation. Meanwhile,
286 inhibition of DBN1 via its inhibitor BTP2 significantly blocked the migration of ICC
287 cells (Fig. 5G). Notably, BTP2 exerted its inhibitory effect by decreasing
288 phosphorylation at Ser142 of DBN1 (Fig. 5H, Fig S16E). Together, these results
289 demonstrate the critical roles of p-mTORC1 and DBN1 Ser142 phosphorylation in the
290 THBS1-mediated migration signalling pathway.

291 Finally, we examined the role of THBS1 in ICC progression by combing the

292 AKT1/NICD1 ICC model with Thbs1$^{fl/fl}$;Lyz-Cre mice (Fig. 5I). Myeloid-specific
293 deletion of *Thbs1* significantly reduced liver-to-body weight ratios and tumour burden,
294 resulting in smaller liver size and fewer, smaller tumour foci (Fig. 5J–K). Western
295 blotting revealed that *Thbs1* deletion was accompanied by significant downregulation
296 of CD47, DBN1, p-DBN1, p-mTORC1, and Vimentin levels in ICC tissues (Fig. 5L).
297 Collectively, these findings establish THBS1 as a master EMT regulator via PI3K-
298 AKT-mTOR activation and DBN1 phosphorylation in ICC.
299

300 **Combined blockade of OSM and THBS1 effectively inhibits ICC progression**

301 Since *OSM* promotes proliferation and *THBS1* enhances invasiveness, we asked
302 whether dual inhibition could synergistically suppress ICC. We analysed *THBS1* and
303 *OSM* expression in 833 patients from 9 ICC/Cholangiocarcinoma cohorts (Table S1),
304 and calculated the mean expression levels of *THBS1* and *OSM* in each cohort. An ICC
305 sample was defined as double-positive if both genes had expression levels greater than
306 the mean value of the cohort. Using this criterion across 9 datasets, the proportion of
307 *THBS1/OSM* double-positive ICC samples ranged from 13.33% to 29.53%, and
308 exceeded 20% in five datasets (Fig. 6A). Next, we genetically ablated macrophage-
309 derived *THBS1* using Thbs1$^{fl/fl}$; Lyz-cre mice and pharmacologically inhibited OSM-
310 OSMR interaction via intraperitoneal administration of OSM-SMI-10B, an OSMR
311 inhibitor.[19] *Thbs1* deletion or *Osmr* inhibition alone suppressed ICC progression
312 moderately, while combined blockade attenuated ICC development more robustly, as
313 evidenced by further reduced tumour burden using H&E staining and a decreased liver-

314 to-body weight ratio (Fig. 6B–D). These results collectively indicate that combined
315 blockade of OSM and THBS1 may generate synergetic therapeutic effects for ICC
316 treatment.
317

318 **Mafb promotes M2 polarisation and enhances *OSM* and *THBS1* expression in**
319 **macrophages**

320 We next examined epigenetic modification in macrophages. Liver tissues from
321 AKT1/NICD1 ICC mice at middle/advanced stages and vector controls were subjected
322 to time-series single cell ATAC sequencing (scATAC-seq) to map regulatory elements
323 in Mφ_VEGFA (Fig. S17A–C). Accessibility profile analysis of cell type markers using
324 ArchR (V1.0.3) and integrated AKT1/NICD1 scRNA-seq and scATACseq data
325 identified seven major cell types (CAF, TEC, EPI, B, NEU, T_NK, and TAMs; Fig. 7A,
326 S17A–B). Further, re-clustering of TAMs revealed three subtypes—Mφ_Clec4f,
327 Mφ_Vegfa, and Mφ_S100a (Fig. 7A, S17C). ArchR to analyze chromatin accessibility
328 and transcription factor (TF) motifs across TAM subtypes revealed that Mφ_Vegfa and
329 Mφ_S100a subsets exhibited markedly distinct regulatory landscapes (Fig. 7B). In
330 Mφ_S100a, the Klf transcription factor family exhibited specific activation (Fig 7B,
331 S17D), with TF *Klf3* showing the highest expression and regulating inflammation
332 response genes including *S100a4* and *S100a8* (Fig. 7C, 7D, S17D, S17E). In
333 comparison, Mφ_Vegfa displayed preferential chromatin accessibility of *Maf*
334 transcription factor family (Fig 7B), with *Mafb* showing the highest expression (Fig.
335 7C). Notably, *Mafb* regulated genes were enriched in cell differentiation pathways—

Mafb was predicted to regulate M2 polarisation markers (*Cd163*, *Mrc1*, *Il10*) and *Osm* (Fig. 7D, S17F). *MAFB* was highly expressed at the tumour boundary in mouse and human ICC tissues and thus overlapped with Mφ_VEGFA localisation (Fig. 7E). *Mafb* also showed significantly increased chromatin accessibility in Mφ_Clec4f (Kupffer cells). Mφ_Clec4f exhibited high accessibility of *Cd163* and *Mrc1* but low expression of *Osm* and *Thbs1* (Fig. S17G), indicating that the regulatory role of *Mafb* on *Osm/Thbs1* is specific to Mφ_VEGFA. Together, these data suggest that *Mafb* plays an important role in regulating macrophage M2 polarisation.

To confirm the role of Mafb in Mφ_Vegfa, we performed cell-cell communication analysis, which revealed that E_Jun ICC subcluster interacted with Mφ_Vegfa in mouse via the Tgfb2-Tgfbr2 ligand-receptor pair, that regulated *Mafb* expression (Fig. S18A–B). In the Transwell co-culture system, *TGFB2* was upregulated in ICC cells, while *Tgfbr2* was upregulated in BMDMs (Fig. S18C). As TGF-β2 regulates M2 polarisation,[20] We found that TCM or recombinant TGF-β2 significantly upregulated the expression of M2 markers in BMDMs, including *Mrc1* (Cd206), *Arg1*, and *Mafb*-regulated genes *Tgfbr2*, *Thbs1*, and *Osm* (Fig 7F, 7G, Fig S18D, E). Crucially, siRNA knockdown of *Mafb* significantly reduced expression of *Arg1, Vegfa, Osm*, and *Thbs1* (Fig. 7H). These results indicate that *MAFB* could regulate macrophage M2 polarisation via *OSM* and *THBS1* signalling.

356 **Discussion**

357 The roles of TAMs in ICC have been linked to poor prognosis through promotion of
358 tumour growth and invasiveness.[21, 22] Recent single-cell omics studies have revealed
359 the molecular diversity and functions of TAMs in cancer,[23] but the specific subgroups
360 driving ICC malignancy and its interactions with tumour cells remain unclear. Using a
361 time-resolved ICC mouse model with integrated multi-omics, we identified
362 Mφ_VEGFA as a poor-prognosis TAM subset in ICC. Spatial transcriptomics
363 confirmed its boundary localisation and functional niche. Mφ_VEGFA displayed
364 mainly M2-like traits with distinct marker genes separating it from other TAMs. Its
365 prognostic significance was also observed in hepatocellular carcinoma (HCC),[11]
366 underscoring relevance across liver cancer, highlighting Mφ_VEGFA as a therapeutic
367 target for both ICC and HCC.[24] Mechanistically, Mφ_VEGFA promotes ICC
368 proliferation and invasion through coordinated multiple pathway via OSM-OSMR
369 signalling, activating STAT3 phosphorylation and CCND1 induction, similar to
370 glioblastoma [25] This observation is consistent with the finding that OSM promotes
371 cancer cell proliferation and differentiation in breast cancer and pancreatic ductal
372 adenocarcinoma.[26] Its pro-invasive function depends on the secreted matricellular
373 glycoprotein THBS1, which activates CD47 signalling in ICC cells. THBS1 derived
374 from tumour-infiltrating monocyte-like cells reportedly induces an immunosuppressive
375 TME and contributes to cancer metastasis.[27] Notably, we demonstrate that *CD47*
376 activates mTOR in ICC cells but not IL6/STAT3, resulting in DBN1 Ser124
377 phosphorylation, as also observed in oral squamous cell carcinoma.[28] While

378 THBS1/CD47 mediate immune evasion, our study reveals its direct role in ICC
379 proliferation and invasion.
380
381 Our findings offer a new therapeutic strategy for ICC treatment aiming at macrophages.
382 OSM/OSMR and THBS1/CD47 axes mediate macrophage-ICC interactions,
383 suggesting their potential as therapeutic targets for ICC. Although administration of
384 single OSM or mTOR inhibitors (blocking CD47 signalling) achieved limited
385 inhibitory effect on ICC growth, combined blockade of OSM-OSMR and
386 THBS1/CD47 signalling generated synergetic anti-tumour effects in an ICC mouse
387 model. Consistently, a clinical trial showed that targeting OSM/OSMR signalling alone
388 led to poor outcome or drug resistance.[29] Thus, targeting dual modulators of
389 Mφ_VEGFA provides a potentially more robust therapeutic option. Further, OSM and
390 THBS1 were concurrently upregulated in 13–29% of patients with ICC and
391 OSM/OSMR and THBS1/CD47 signalling promoted ICC proliferation and migration,
392 respectively. Therefore, combination therapy targeting these two signalling pathways
393 may be effective in patients with ICC at different stages.
394 Lastly, our study indicates that Mφ_VEGFA polarisation is dependent on MafB and
395 demonstrates a metabolic profile with highly active lipid metabolism. MafB has been
396 reported with c-Maf functioning as a self-renewal blocker in monocytes and
397 macrophages, and deficiency of these two genes enables extended expansion of mature
398 monocytes and macrophages in culture while maintaining their differentiated
399 phenotype and function.[30] In addition, macrophages express acute inflammatory

response genes in a Maf-dependent manner upon bacteria exposure and simultaneously downregulate Maf through accelerated degradation via the proteasome pathway and microRNA-mediated silencing.[31] In this study, we further demonstrate that MAF is required for macrophage polarisation in the TME and highlight the roles of MAF in orchestrating macrophage activation and polarisation.

Abbreviations

TAMs, tumour-associated macrophages; ICC, intrahepatic cholangiocarcinoma; TME, tumour microenvironment; EMT, epithelial mesenchymal transition; Mal, malignant tumour cells region; Bdy, tumour boundary; nMal, adjacent non-malignant region; B, B cells; DC, dendritic cells; CAF, cancer-associated fibroblasts; CHO, cholangiocyte; HPE, hepatocyte; T_NK, T and NK cells; TEC, tumour endothelial cells. NEU, neutrophils. EPI, epithelial cells. BMDMs, bone marrow–derived macrophages. scRNAseq, single cell RNA sequencing; spRNAseq, spatial transcriptomics sequencing; scATACseq, single cell ATAC sequencing.

Acknowledgements

This work was financially supported by the National Natural Science Foundation of China (Grant No. 82472988, 82403200, 82372667, 82273059 and 82573814). We sincerely thank them for their generous support.

References

[1] Moris D, Palta M, Kim C, et al. Advances in the treatment of intrahepatic cholangiocarcinoma: An overview of the current and future therapeutic landscape for clinicians. CA: a cancer journal for clinicians 2023;73:198-222. https://doi.org/10.3322/caac.21759

[2] Greten TF, Schwabe R, Bardeesy N, et al. Immunology and immunotherapy of cholangiocarcinoma. Nat Rev Gastroenterol Hepatol 2023;20:349-365. https://doi.org/10.1038/s41575-022-00741-4.

[3] Zhou M, Wang C, Lu S, et al. Tumor-associated macrophages in cholangiocarcinoma: complex interplay and potential therapeutic target. EBioMedicine 2021;67:103375. https://doi.org/10.1016/j.ebiom.2021.103375.

[4] Guan F, Wang R, Yi Z, et al. Tissue macrophages: origin, heterogenity, biological functions, diseases and therapeutic targets. Signal Transduct Target Ther 2025;10:93. https://doi.org/10.1038/s41392-025-02124-y.

[5] Chen S, Saeed A, Liu Q, et al. Macrophages in immunoregulation and therapeutics. Signal Transduct Target Ther 2023;8:207. https://doi.org/10.1038/s41392-023-01452-1.

[6] Fan G, Tao C, Li L, et al. The co-location of MARCO+ tumor-associated macrophages and CTSE+ tumor cells determined the poor prognosis in intrahepatic cholangiocarcinoma. Hepatology 2025;82:25-41. https://doi.org/10.1097/HEP.0000000000001138.

[7] Song G, Shi Y, Meng L, et al. Single-cell transcriptomic analysis suggests two molecularly subtypes of intrahepatic cholangiocarcinoma. Nat Commun 2022;13:1642. https://doi.org/10.1038/s41467-022-29164-0.

[8] Li Z, Li Zhao, Chen Q, et al. Single-Cell and Spatial Transcriptomics Delineate the Microstructure and Immune Landscape of Intrahepatic Cholangiocarcinoma in the Leading-Edge Area. Ad Sci 2025;12:e2412740. https://doi.org/10.1002/advs.202412740.

[9] Yan J, Jiang Z, Zhang S, et al. Spatial–temporal heterogeneities of liver cancer and the discovery of the invasive zone. Clin Transl Med 2025;15:e70224. https://doi.org/10.1002/ctm2.70224.

[10] Dong LQ, Shi Y, Ma LJ, et al. Spatial and temporal clonal evolution of intrahepatic cholangiocarcinoma. J Hepatol 2018;69:89-98. https://doi.org/10.1016/j.jhep.2018.02.029.

[11] Zhang Q, He Y, Luo N, et al. Landscape and Dynamics of Single Immune Cells in Hepatocellular Carcinoma. Cell 2019;179:829-845.e820. https://doi.org/10.1016/j.cell.2019.10.003.

[12] Su X, Liang C, Chen R, et al. Deciphering tumor microenvironment: CXCL9 and SPP1 as crucial determinants of tumor-associated macrophage polarity and prognostic indicators. Mol Cancer 2024;23:13. https://doi.org/10.1186/s12943-023-01931-7.

[13] Jusakul A, Cutcutache I, Yong CH, et al. Whole-Genome and Epigenomic Landscapes of Etiologically Distinct Subtypes of Cholangiocarcinoma. Cancer Discov 2017;7:1116-1135. https://doi.org/10.1158/2159-8290.CD-17-0368.

[14] Ahn KS, O'Brien D, Kang YN, et al. Prognostic subclass of intrahepatic cholangiocarcinoma by integrative molecular-clinical analysis and potential targeted approach. Hepatol Int 2019;13:490-500. https://doi.org/10.1007/s12072-019-09954-3.

[15] Lubuela G, Beaufrere A, Albuquerque M, et al. Prognostic impact of the tumour microenvironment in intrahepatic cholangiocarcinoma: identification of a peritumoural fibro-immune interface. Virchows Arch 2024;485:901-911. https://doi.org/10.1007/s00428-024-03922-5.

[16] Wu R, Guo W, Qiu X, et al. Comprehensive analysis of spatial architecture in primary liver cancer. Sci Adv 2021;7:eabg3750. https://doi.org/10.1126/sciadv.abg3750.

[17] Low J, Altman R, Badolian A, et al. Heat-induced phosphatidylserine changes drive HSPA1A's plasma membrane localization. Cell Stress Chaperones 2025;30. https://doi.org/10.1016/j.cstres.2025.100092.

[18] Shashikanth N, Alaidi O, Basa L, et al. Role of C-Jun N-Terminal Kinases on a Stressed Epithelium: Time for Testing Isoform Specificity. Biology 2025;14. https://doi.org/10.3390/biology14060649.

[19] Wolf CL, Feci A, Tuccinardi JP, et al. Development of the First Small-Molecule Inhibitor Targeting Oncostatin M for Treatment of Breast Cancer. J Med Chem 2025;68:15422-15445. https://doi.org/10.1021/acs.jmedchem.4c03233

[20] Luo L, Wang S, Hu Y, et al. Precisely Regulating M2 Subtype Macrophages for Renal Fibrosis Resolution. ACS Nano 2023;17:22508-22526. https://doi.org/10.1021/acsnano.3c05998.

[21] Hasita H, Komohara Y, Okabe H, et al. Significance of alternatively activated macrophages in patients with intrahepatic cholangiocarcinoma. Cancer Sci 2010;101:1913-1919. https://doi.org/10.1111/j.1349-7006.2010.01614.x.

[22] Hui Y, Lin Z, Liu Y, et al. Intrahepatic cholangiocarcinoma induced M2-polarized tumor-associated macrophages facilitate tumor growth and invasiveness. Cancer Cell Int 2020;20:586. https://doi.org/10.1186/s12935-020-01687-w.

[23] Ma RY, Black A, Qian BZ. Macrophage diversity in cancer revisited in the era of single-cell omics. Trends Immunol 2022;43:546-563. https://doi.org/10.1016/j.it.2022.04.008.

[24] Okikawa S, Morine Y, Saito Y, et al. Inhibition of the VEGF signaling pathway attenuates tumor-associated macrophage activity in liver cancer. Oncol Rep 2022;47:71. https://doi.org/10.3892/or.2022.8282.

[25] Chen M, Ren R, Lin W, et al Exploring the oncostatin M (OSM) feed-forward signaling of glioblastoma via STAT3 in pan-cancer analysis. Cancer Cell Int 2021;21:565. https://doi.org/10.1186/s12935-021-02260-9.

[26] Polak KL, Tamagno I, Parameswaran N, et al. Oncostatin-M and OSM-Receptor Feed-Forward Activation of MAPK Induces Separable Stem-like and Mesenchymal Programs. Mol Cancer Res 2023;21:975-990. https://doi.org/10.1158/1541-7786.MCR-22-0715.

[27] Omatsu M, Nakanishi Y, Iwane K, et al. THBS1-producing tumor-infiltrating monocyte-like cells contribute to immunosuppression and metastasis in colorectal cancer. Nat Commun 2023;14:5534. https://doi.org/10.1038/s41467-023-41095-y.

[28] You Y, Tian Z, Du Z, et al. M1-like tumor-associated macrophages cascade a mesenchymal/stem-like phenotype of oral squamous cell carcinoma via the IL6/Stat3/THBS1 feedback loop. J Exp Clin Cancer Res 2022;41:10. https://doi.org/10.1186/s13046-021-02222-z.

[29] Wolf CL, Pruett C, Lighter D, et al. The clinical relevance of OSM in inflammatory diseases: a comprehensive review. Front Immunol 2023;14:1239732. https://doi.org/10.3389/fimmu.2023.1239732.

[30] Aziz A, Soucie E, Sarrazin S, et al. MafB/c-Maf deficiency enables self-renewal of differentiated functional macrophages. Science 2009;326:867-871. https://doi.org/10.1126/science.1176056.

[31] Kikuchi K, Iida M, Ikeda N, et al. Macrophages Switch Their Phenotype by Regulating Maf Expression during Different Phases of Inflammation. J Immunol 2018;201:635-651. https://doi.org/10.4049/jimmunol.1800040.

505

506 **Figure legends**

507 **Fig. 1. Spatiotemporal heterogeneity of macrophages in mouse and human ICC tissues.**(A) (i)
508 UMAP visualisation of TAMs from patients with ICC p (datasets GSE138709 and GSE189903). (ii)
509 Stacked bar plots showing the distribution of TAM subclusters across malignant (Mal), boundary
510 (Bdy), and adjacent non-malignant (nMal) regions. (B) (i) UMAP of TAM subclusters in
511 AKT1/NICD1 mice. (ii) Scatter plot of M2 polarisation scores of TAMs. (iii) Temporal distribution
512 of TAM subtype, WT (healthy, N=2), D7 (early stage, N=2), D15 (middle stage, N=3), D25 (middle
513 to advanved stage, N=2), D31 (advanced stage, N=3). (C) Bubble plots displaying the expression
514 of TAM marker genes in patients with ICC and the AN model. Color indicates expression levels,
515 bubble size reflects cell proportion. (D) (i) Temporal dynamics of TAM subclusters in the AN model.
516 (ii) Mφ_S100a and Mφ_Vegfa scores across the time axis, with red indicating mean expression
517 levels above the 90th percentile. (E) Scatter–pie plots illustrating prognostic associations of distinct
518 TAM subclusters. Pie chart illustrating cell prognosis outcomes in each TAM subtype. Blue, survival.
519 Red, death. Grey, no significant association.(F) (i) Overview of in vivo study with FVB mice. (ii)
520 Macrophage infiltration levels ($CD11b^+F4/80^+$ cells within $CD45^+$ population; $F4/80^+$ cells within
521 $CD11b^+$ population) analyzed via flow cytometry and correlated with liver-to-body weight ratio
522 using scatter plots and correlation analysis. Data are presented as mean ± SD. Significance was
523 determined by two-tailed unpaired t-test (**$p < 0.01$).(G) (i) Spatial segments of AKT1/NICD1
524 tissue. (ii) Stacked bar plots showing cell-type composition across spatial clusters (xCell). (iii)
525 Contour maps highlighting spatial expression of Mφ_Vegfa. (iv) Spatial distribution of *Mrc1*
526 (*Cd206*) and F4/80 (*Adgre1*) in AKT1/NICD1 tissue. (H) (i) Spatial transcriptomics identified seven
527 cell populations in human tissue. (ii) RCTD-based analysis of cellular composition across spatial

528 domains; (iii) Scatter plot showing cell functional regions predicted by Cottrazm. (iv) Contour maps
529 of Mφ_VEGFA. (v) Spatial distribution of *MRC1*. spRNAseq, spatial RNA sequencing.
530
531 **Fig. 2. Mφ_VEGFA promotes ICC proliferation via OSM-OSMR.** (A) UMAP plot (left) and
532 bubble plot (right) illustrating the distribution of epithelial cells in AKT1/NICD1 mice and the
533 profile of their corresponding cell type features. (B) UMAP plots showing the patients' epithelial
534 subtypes. (C) Venn diagram showing overlap of ligand genes that are significantly upregulated in
535 Mφ_VEGFA which exhibit strong interactions with tumor cells as identified by three cell
536 communication methods (CellphoneDB,CpDB; CellChat, and NicheNet). (D) Heatmap showing the
537 interaction intensity between TAMs and tumour cells in AKT1/NICD1-mediated *OSM* signalling.
538 Bar illustrates interaction probability. (E) Bubble chart visualising pathway enrichment for
539 downstream target genes of *OSM* in E_Jun (AN) and E_CD74 (Human) via NicheNet. Bubble size
540 depicts enrichment score and colour showcasing significance (-log10(p.adj), Clusterprofiler). (F)
541 Schematic of in vivo experimental design. Representative images of livers from $Lifr^{fl/fl}$ and $Osmr^{fl/fl}$
542 control mice and $Lifr^{fl/fl}$;Alb-Cre and $Osmr^{fl/fl}$;Alb-Cre mice injected with AKT1/NICD1. (G) Bar
543 graphs showing liver-to-body weight ratios analysis of Osmr and Lifr transcript levels in liver tissues
544 from $Lifr^{fl/fl}$, $Lifr^{fl/fl}$;Alb-Cre, $Osmr^{fl/fl}$, and $Osmr^{fl/fl}$;Alb-Cre mice injected with AKT1/NICD1. Data
545 are presented as mean ± SD. Statistical significance was analyzed by one-way ANOVA ($p < 0.05$)
546 followed by Dunnett's test (ns, not significant, $^{**}p < 0.01$, $^{***}p < 0.001$; $^{****}p < 0.0001$). (H)
547 Multiplex immunofluorescence showing spatial co-localisation between $CD68^{+}OSM^{+}$ TAMs and
548 $OSMR^{+}KRT19^{+}$ tumour cells in ICC patients. Scale bar, 200 μm.
549

550 **Fig. 3. Mφ_VEGFA promotes ICC proliferation by upregulating p-STAT3 and CCND1 in ICC**
551 **cells.** (A) Bar plot showing gene expression levels in co-culture. Statistical significance was
552 analyzed by one-way ANOVA ($p < 0.05$) followed by Dunnett's test (ns, not significant, $^{**}p < 0.01$,
553 $^{***}p < 0.001$; $^{****}p < 0.0001$). R, Raw264.7. Q, QBC939. (B) CCK-8 assay measuring cell
554 viability of HuCCT1 and QBC939 cells treated with 2.5 ng/mL or 5.0 ng/mL OSM, or left untreated,
555 for 5 consecutive days. (C) (i) EdU incorporation assay in QBC939 cells transduced with control
556 vector or OSMR-targeting sgRNAs (sgOSMR-1, sgOSMR-2). (ii) CCK-8 assay measuring viability
557 of HuCCT1 and QBC939 cells transduced with control vector or sgOSMR-1 at days 1, 3, and 5 after
558 seeding. (iii) Colony formation assay with crystal violet staining of HuCCT1 and QBC939 cells
559 transduced with control vector or sgOSMR-1. Scale bar, 200 μm. (D) Bar plot showing KEGG
560 pathway enrichment among proteins with differential phosphorylation after OSM treatment in
561 QBC939 cells. Blue, downregulation; Red, upregulation. (E) Network showing OSMR pathways.
562 (F) H&E staining and IHC staining for OSMR, OSM, CK19, and Ki-67 in paraffin-embedded liver
563 sections from $Osmr^{fl/fl}$ and $Osmr^{fl/fl}$; Alb-Cre mice injected with AKT1/NICD1. Scale bar, 200 μm.
564 (G) Western blot analysis of OSMR, CCND1, BCL2, phosphorylated STAT3 (p-STAT3),
565 phosphorylated mTORC1 (p-mTORC1), and OSM protein levels in liver tissues from $Osmr^{fl/fl}$ and
566 $Osmr^{fl/fl}$; Alb-Cre; mice injected with AKT1/NICD1. GAPDH served as a loading control. Data are
567 presented as mean ± SD. Significance was determined by two-tailed unpaired t-test ($^{***}p < 0.001$)
568 for B and C.
569
570 **Fig. 4. Mφ_Vegfa promotes ICC invasion via *THBS1-CD47* signaling.** (A) (i) Heatmap of
571 interactions between TAMs and tumor subtypes in THBS1 signaling. Sender,ligand source. Receiver,

572 receptor. Color intensity indicates importance. (ii) Top, bar plot showing receive contributions of
573 ligand THBS1. Bottom row shows *Cd47* expression across epithelial subclusters in AKT1/NICD1
574 data (iii) Spatial patterns of *THBS1-CD47* interaction. (B) Bubble chart visualising pathway
575 enrichment for downstream target genes of *THBS1* in E_Jun (AKT1/NICD1 mouse) and E_IGFBP7
576 (Human) via NicheNet. Bubble size depicts enrichment score and colour showcasing significance
577 (-log10(p.adj), clusterProfiler). (C) Representative scratch wound healing images of HuCCT1 cells
578 treated with 10 ng/mL Thbs1 or control at 0 h, 12 h, and 24 h; and RBE cells treated with 10 ng/mL
579 Thbs1 or control at 0 h, 36 h, and 72 h. Scale bar, 150 μm. (D) Representative crystal violet–stained
580 Transwell migration images of primary BR cells and HuCCT1 cells treated with 10 ng/mL THBS1
581 or control. Scale bar, 150 μm. (E) qRT-PCR analysis of *CD47* levels in HuCCT1 cells transfected
582 with siScramble control, siCD47-1, or siCD47-2 for 48 h. Data are presented as mean ± SD.
583 Statistical significance was analyzed by one-way ANOVA ($p < 0.05$) followed by Dunnett's test
584 (****$p < 0.0001$).(F) Representative crystal violet–stained Transwell migration images of HuCCT1
585 cells transfected with siScramble or siCD47-2. Scale bar, 150 μm. (G) qRT-PCR and western blot
586 analyses of CD47 transcript and protein levels, respectively, in BR cells transduced with LV3-shNC
587 control lentivirus or LV3-shCD47; gene silencing efficiency confirmed by qRT-PCR and western
588 blot. (H) EdU incorporation assay assessing proliferation of BR cells transduced with LV3-shNC or
589 LV3-shCD47 lentivirus. Scale bar, 50 μm. (I) Colony formation assay comparing BR cells
590 transduced with LV3-shNC or LV3-shCd47 lentivirus. (J) CCK-8 assay measuring cell growth of
591 BR cells transduced with LV3-shNC or LV3-shCd47 lentivirus from day 1 to day 5 after seeding.
592 (K) Representative crystal violet–stained Transwell migration images and corresponding chamber
593 images of BR cells transduced with LV3-shNC or LV3-shCd47 co-cultured with BMDMs or

594 cultured with complete medium for 24 h. Scale bar, 150 μm. (L) Subcutaneous allograft tumour
595 growth curves and representative tumour images of BR cells transduced with LV3-shNC or LV3-
596 shCd47 lentivirus. (M) Representative images of mouse abdominal phenotypes at tumour endpoint
597 after intraperitoneal injection of BR cells transduced with LV3-shNC or LV3-shCd47; tumour sites
598 indicated by white arrows; quantification of metastatic nodules and volume of ascites collected.
599 Data are presented as mean ± SD. Significance was determined by two-tailed unpaired t-test (***p
600 < 0.001) for E, G, J and L.
601
602 **Fig. 5. Mφ_Vegfa promotes ICC invasion via mTOR-mediated phosphorylation of DBN1.** (A)
603 Western blotting shows the expression of p-mTOR, p-RPS6, EpCAM, N-cadherin, Vimentin, and
604 the internal control GAPDH in HuCCT1 cells after THBS1 protein stimulation. (B) Bar plot
605 displaying pathway enrichment analysis for HuCCT1 at 6 h and 2 h following the addition of
606 exogenous THBS1 protein. (C) Circos plot displaying differentially phosphorylated sites at multiple
607 time points after adding exogenous THBS1. From inner to outer rings: phosphorylation-site
608 proportions, phosphopeptide expression intensity (inner heatmap), sample groups, and enriched
609 signaling pathways; the outermost ring lists gene symbols and phosphosites unique to each treatment.
610 Colored links show shared phosphosites-gray, common to control and treatments. Brown, mTOR-
611 related. Red, fibrosis-related. Green, mesenchymal-related. Large and small ticks denote 50 and 5
612 phosphopeptides, respectively. (D) Western blot analysis of DBN1, phosphorylated DBN1 (p-
613 DBN1), and Vimentin protein levels in BR cells cultured alone or co-cultured with BMDMs for 24
614 h or 48 h; GAPDH served as a loading control. (E) Representative crystal violet–stained images
615 from Transwell migration assays of HuCCT1 and BR cells co-cultured with BMDMs, with or

without Rapamycin treatment. N = 5. Scale bar, 200 μm. (F) Representative crystal violet–stained images from Transwell migration assays of HuCCT1 and BR cells treated with THBS1, with or without Rapamycin blockade; groups include control, THBS1 treatment, and THBS1 combined with Rapamycin. N = 5. Scale bar, 200 μm. (G) Representative chamber and crystal violet–stained images of Transwell migration assays for HuCCT1 cells (i) treated with 0, 5, 25, and 125 μM BTP2 inhibitor, and BR cells (ii) treated with 0, 25, and 125 μM BTP2 in the lower chamber. Scale bar, 200 μm. (H) Western blot analysis of phosphorylated DBN1 (p-DBN1, Ser142), total DBN1, phosphorylated mTOR (p-mTOR, Ser2448), Vimentin, CD47, and GAPDH protein levels in HuCCT1 and RBE cells treated with 50 μM BTP2 for 24 h. (I) Schematic of AKT1/NICD1-induced ICC mouse model established by hydrodynamic tail vein injection in $Thbs1^{fl/fl}$;Lyz-Cre and $Thbs1^{fl/fl}$ mice. (J) Representative images of liver phenotypes and quantification of liver-to-body weight ratios in $Thbs1^{fl/fl}$;Lyz-Cre and $Thbs1^{fl/fl}$ mice injected with AKT1/NICD1. Data are presented as mean ± SD. Significance was determined by two-tailed unpaired t-test (*$p < 0.05$), N = 6. (K) H&E staining of liver sections showing whole-slide and magnified tumour areas. Scale bar, 100 μm. (L) Western blot analysis of THBS1, CD47, DBN1, p-DBN1, phosphorylated mTOR (p-mTOR, Ser2448), and Vimentin protein expression in tumour tissues from $Thbs1^{fl/fl}$;Lyz-Cre and $Thbs1^{fl/fl}$ mice injected with AKT1/NICD1; GAPDH served as loading control.AN, AKT1/NICD1.

Fig. 6. Combined intervertion with OSM inhibitor and THBS1 knockout effectively delays ICC progression. (A) Stacked bar plot illustrating the prevalence of $OSM^{+}THBS1^{+}$ dual-positive patients within distinct ICC cohorts. (B) Representative liver phenotype images from four experimental groups in the *THBS1/OSM* combination blockade experiment: (1) $Thbs1^{fl/fl}$ + vehicle

control; (2) Thbs1$^{fl/fl}$ + OSM-SMI-10B; (3) Thbs1$^{fl/fl}$; Lyz2-Cre + vehicle control; (4) Thbs1$^{fl/fl}$; Lyz2-Cre + OSM-SMI-10B. (C) Statistical analysis of liver-to-body weight ratio across different treatment groups in the *THBS1/OSM* combination blockade experiment. Data are presented as mean ± SD. Statistical significance was analysed by one-way ANOVA ($p < 0.05$) followed by Dunnett's test (*$p < 0.05$, **$p < 0.01$, ***$p < 0.001$; ****$p < 0.0001$). (D) H&E and IHC staining of liver sections from the *THBS1/OSM* combination blockade experiment. Ki67 and Ck19 positively identifies ICC tumour nest regions. Scale bar, 200 μm.

Fig. 7. Epigenetic regulatory profile of ICC TAM subtypes and key regulators in Mφ_Vegfa. (A) (i) UMAP of major subtypes identified by scATAC-seq in AKT1/NICD1. (ii) Chromatin accessibility of representative marker genes for each cell type. (B) Volcano plot showing differences in motif deviation scores (chromVAR) between Mφ_S100a and Mφ_Vegfa macrophage subclusters. X-axis: mean motif difference; Y-axis: -log10(FDR). Red dots mark the top 10 transcription factors with the largest accessibility changes (mean difference > 0.05, FDR < 0.05; Wilcoxon test in ArchR). (C) (i) Venn diagram showing transcription factors with the most distinct motifs between the two subclusters and their overlap with factors expressed >1. (ii) UMAP scatter plots depicting chromatin accessibility distribution for representative differential motifs. (D) Bubble plots depicting pathway enrichment of putative target genes regulated by transcription factors *Klf3* in Mφ_S100a(i) and *Mafb* in Mφ_Vegfa(ii). (E) Spatial expression patterns of the key transcription factor *MAFB* in AKT1/NICD1 mice and human tissues. (F) qRT-PCR analysis of *Tgfbr2*, *Mafb*, *Thbs1*, and *Osm* after BMDM polarising with TCM for 2, 6, 12, 24, 36, and 48 hours. (G) qRT-PCR evaluating *Tgfbr2, Mafb, Thbs1*, and *Osm* transcript levels under different culture conditions. (H) qRT-PCR

analysis of *Arg1, Vegfa, Osm*, and *Thbs1* in siScramble non-polarised, siScramble TCM polarised, and siMafb-1 or siMafb-2 TCM treated groups. Data are presented as mean ± SD. Statistical significance was analysed by one-way ANOVA ($p < 0.05$) followed by Dunnett's test (*$p < 0.05$, **$p < 0.01$, ***$p < 0.001$; ****$p < 0.0001$) for F, G and H.

Figures

Fig.1.

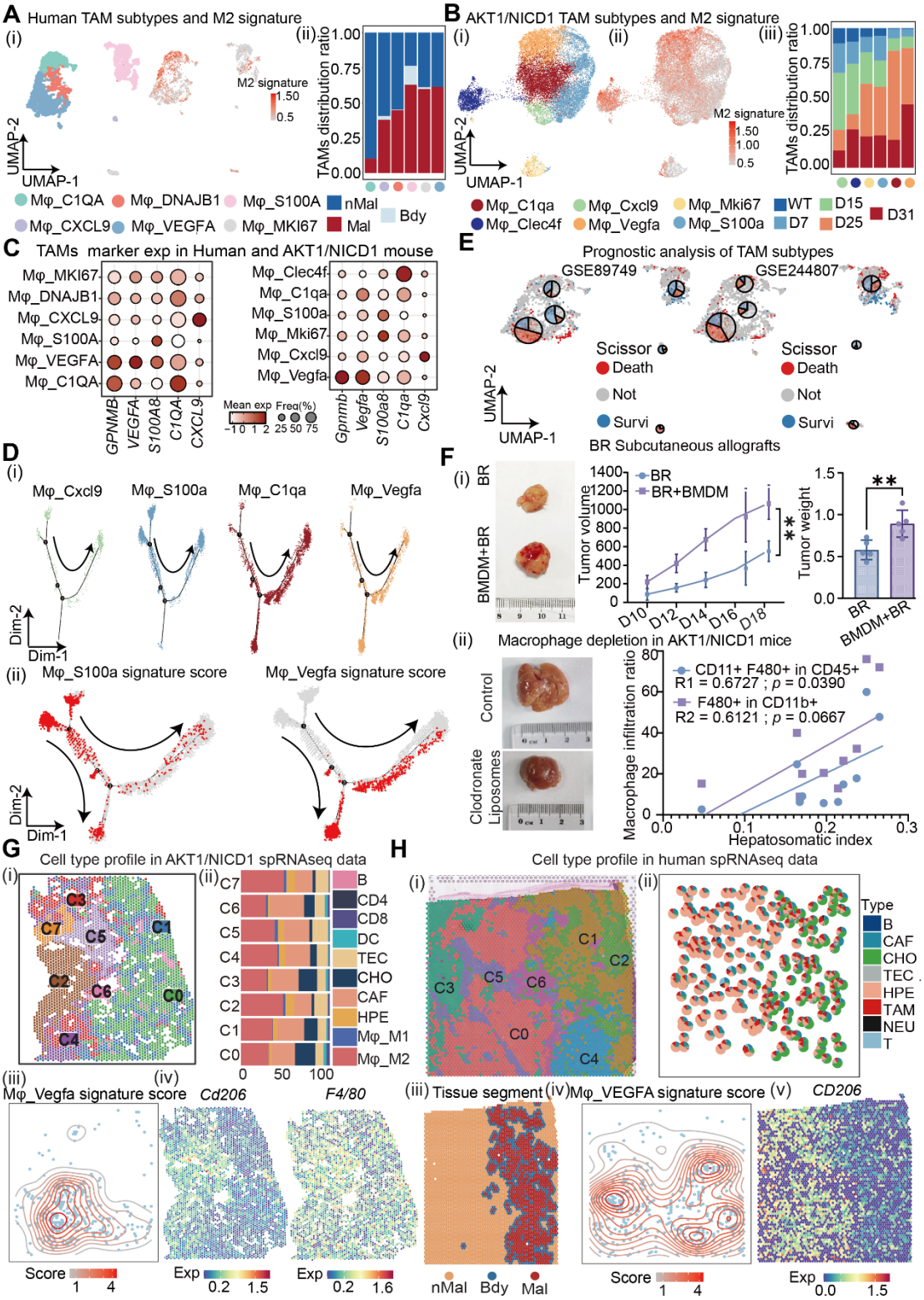

Fig. 2.

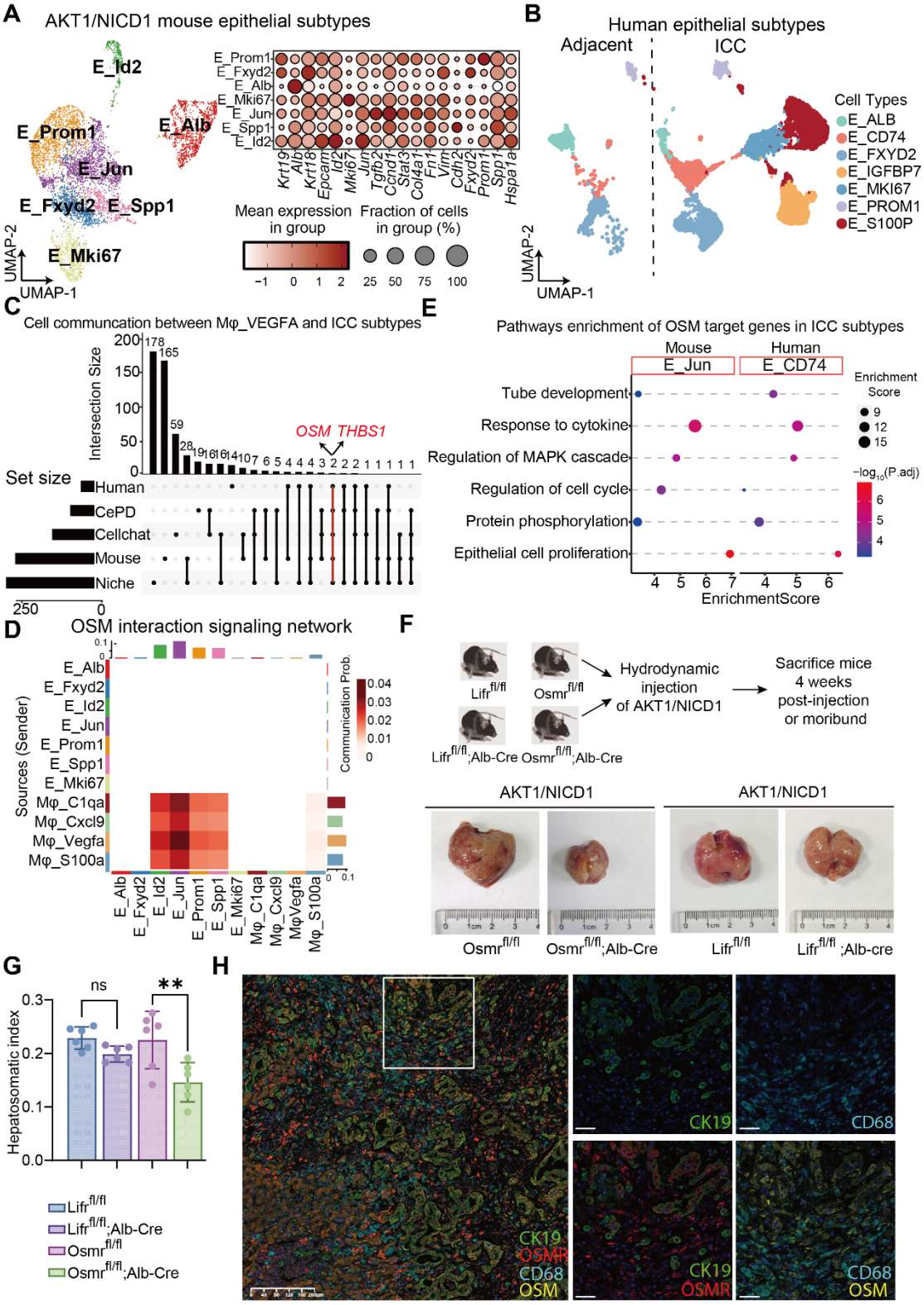
A
AKT1/NICD1 mouse epithelial subtypes
E_Id2
E_Prom1
E_Alb
E_Jun
E_Fxyd2
E_Spp1
E_Mki67
UMAP-2
UMAP-1
Mean expression in group
Fraction of cells in group (%)
B
Human epithelial subtypes
Adjacent
ICC
Cell Types
E_ALB
E_CD74
E_FXYD2
E_IGFBP7
E_MKI67
E_PROM1
E_S100P
C
Cell communcation between Mφ_VEGFA and ICC subtypes
Intersection Size
Set size
Human
CePD
Cellchat
Mouse
Niche
OSM THBS1
E
Pathways enrichment of OSM target genes in ICC subtypes
Mouse
Human
E_Jun
E_CD74
Tube development
Response to cytokine
Regulation of MAPK cascade
Regulation of cell cycle
Protein phosphorylation
Epithelial cell proliferation
Enrichment Score
EnrichmentScore
D
OSM interaction signaling network
Sources (Sender)
Communication Prob.
F
Lifr fl/fl
Osmr fl/fl
Lifr fl/fl;Alb-Cre
Osmr fl/fl;Alb-Cre
Hydrodynamic injection of AKT1/NICD1
Sacrifice mice 4 weeks post-injection or moribund
AKT1/NICD1
G
Hepatosomatic index
ns
**
H
CK19
CD68
OSMR
OSM

Fig. 3.

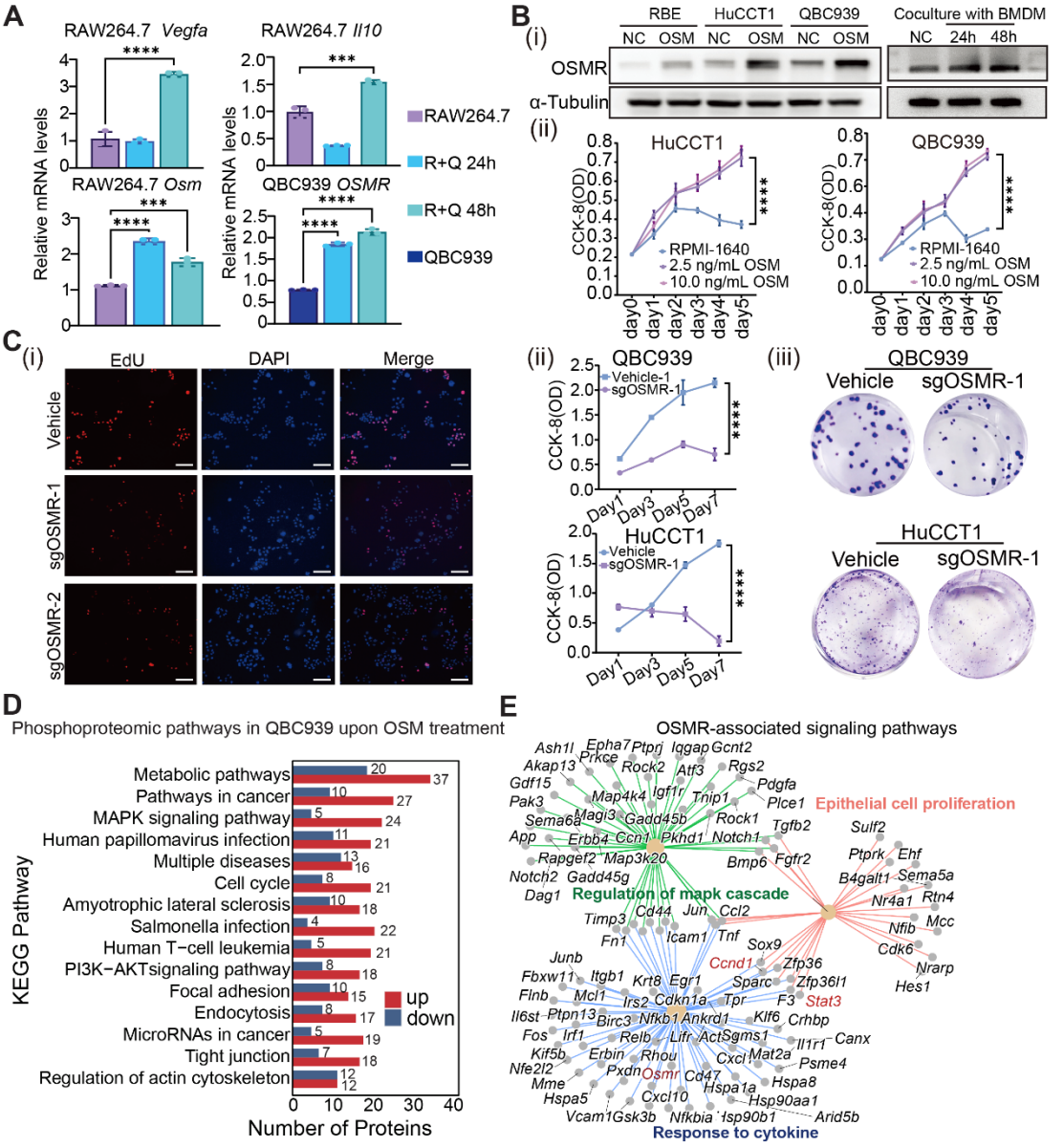
A
RAW264.7 Vegfa
RAW264.7 Il10
RAW264.7 Osm
QBC939 OSMR
Relative mRNA levels
RAW264.7
R+Q 24h
R+Q 48h
QBC939
B
(i)
RBE
HuCCT1
QBC939
Coculture with BMDM
NC
OSM
24h
48h
OSMR
α-Tubulin
(ii)
HuCCT1
QBC939
CCK-8(OD)
RPMI-1640
2.5 ng/mL OSM
10.0 ng/mL OSM
C
(i)
EdU
DAPI
Merge
Vehicle
sgOSMR-1
sgOSMR-2
(ii)
QBC939
Vehicle-1
sgOSMR-1
HuCCT1
Vehicle
(iii)
QBC939
Vehicle
sgOSMR-1
HuCCT1
Vehicle
sgOSMR-1
D
Phosphoproteomic pathways in QBC939 upon OSM treatment
KEGG Pathway
Metabolic pathways
Pathways in cancer
MAPK signaling pathway
Human papillomavirus infection
Multiple diseases
Cell cycle
Amyotrophic lateral sclerosis
Salmonella infection
Human T-cell leukemia
PI3K-AKTsignaling pathway
Focal adhesion
Endocytosis
MicroRNAs in cancer
Tight junction
Regulation of actin cytoskeleton
up
down
Number of Proteins
E
OSMR-associated signaling pathways
Epithelial cell proliferation
Regulation of mapk cascade
Response to cytokine
F
H&E
OSMR
OSM
CK19
Ki-67
Osmr fl/fl AKT1/NICD1
Osmr fl/fl;Alb-cre AKT1/NICD1
G
Osmr fl/fl AKT1/NICD1
Osmr fl/fl;Alb-cre AKT1/NICD1
OSMR
CCND1
BCL2
p-STAT3
p-mTOR
OSM
GAPDH

Fig. 4.

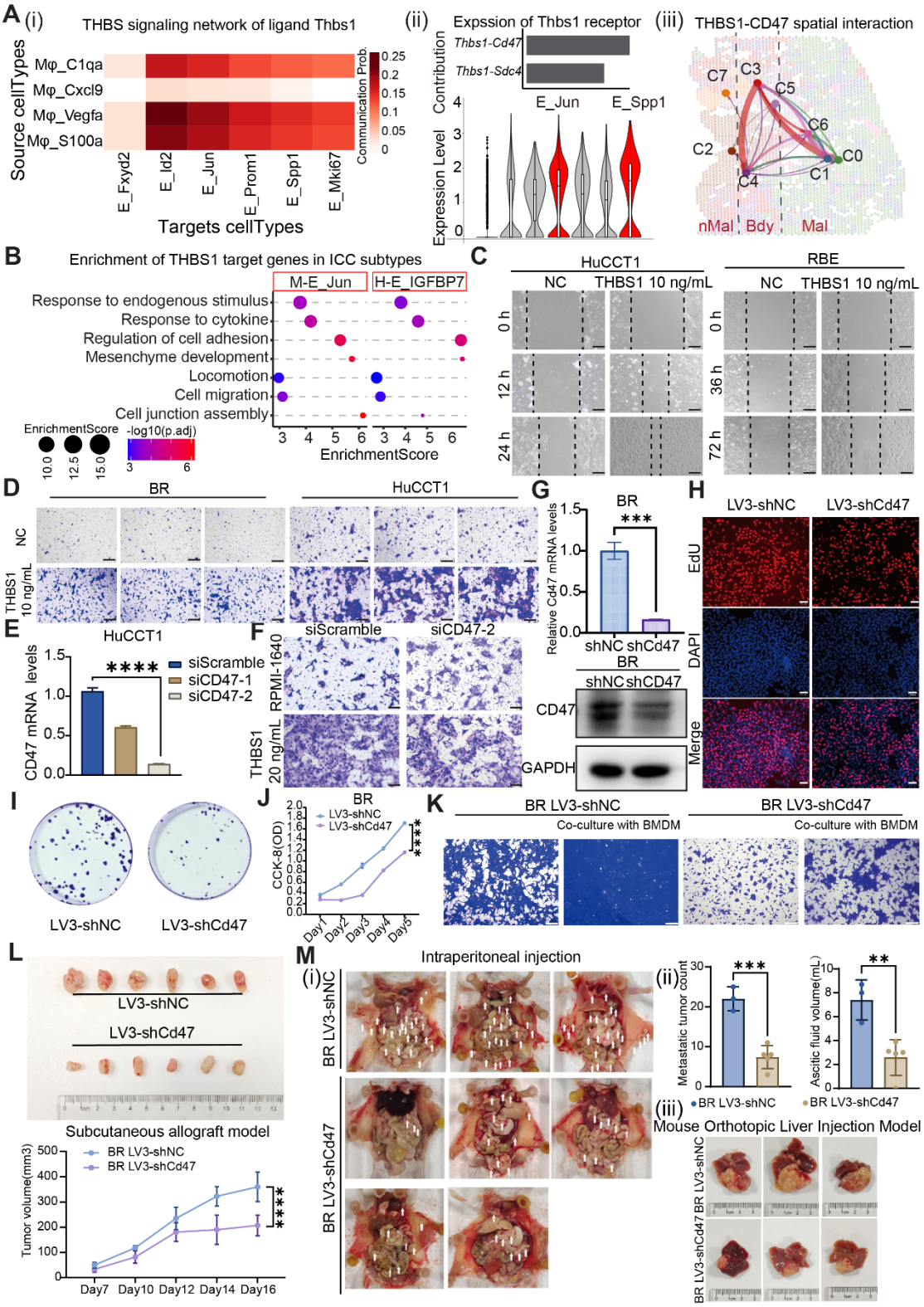
A (i) THBS signaling network of ligand Thbs1
Source cellTypes
Mφ_C1qa
Mφ_Cxcl9
Mφ_Vegfa
Mφ_S100a
E_Fxyd2
E_Id2
E_Jun
E_Prom1
E_Spp1
E_Mki67
Targets cellTypes
Communication Prob.
(ii) Expssion of Thbs1 receptor
Thbs1-Cd47
Thbs1-Sdc4
Contribution
E_Jun
E_Spp1
Expression Level
(iii) THBS1-CD47 spatial interaction
C7
C3
C5
C6
C2
C0
C4
C1
nMal
Bdy
Mal
B Enrichment of THBS1 target genes in ICC subtypes
M-E_Jun
H-E_IGFBP7
Response to endogenous stimulus
Response to cytokine
Regulation of cell adhesion
Mesenchyme development
Locomotion
Cell migration
Cell junction assembly
EnrichmentScore
-log10(p.adj)
C
HuCCT1
RBE
NC
THBS1 10 ng/mL
0 h
12 h
24 h
36 h
72 h
D
BR
HuCCT1
NC
THBS1 10 ng/mL
E
HuCCT1
CD47 mRNA levels
siScramble
siCD47-1
siCD47-2
F
siScramble
siCD47-2
RPMI-1640
THBS1 20 ng/mL
G
BR
Relative Cd47 mRNA levels
shNC
shCd47
CD47
GAPDH
H
LV3-shNC
LV3-shCd47
EdU
DAPI
Merge
I
LV3-shNC
LV3-shCd47
J
BR
LV3-shNC
LV3-shCd47
CCK-8(OD)
Day1
Day2
Day3
Day4
Day5
K
BR LV3-shNC
BR LV3-shCd47
Co-culture with BMDM
L
LV3-shNC
LV3-shCd47
Subcutaneous allograft model
BR LV3-shNC
BR LV3-shCd47
Tumor volume(mm3)
Day7
Day10
Day12
Day14
Day16
M
Intraperitoneal injection
(i)
BR LV3-shNC
BR LV3-shCd47
(ii)
Metastatic tumor count
Ascitic fluid volume(mL)
BR LV3-shNC
BR LV3-shCd47
(iii)
Mouse Orthotopic Liver Injection Model
BR LV3-shNC
BR LV3-shCd47

Fig. 5.

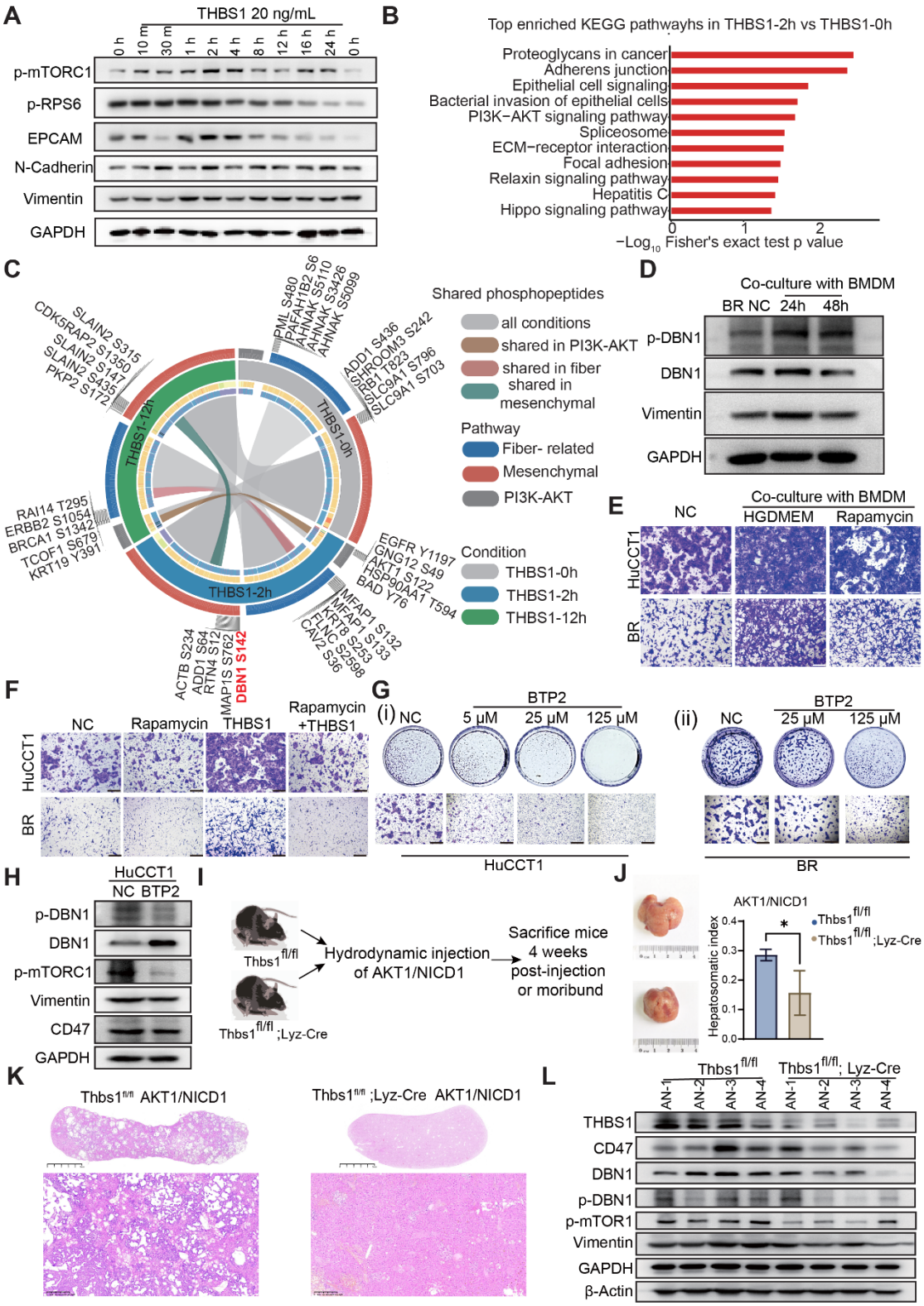

A
THBS1 20 ng/mL
0 h
10 m
30 m
1 h
2 h
4 h
8 h
12 h
16 h
24 h
0 h
p-mTORC1
p-RPS6
EPCAM
N-Cadherin
Vimentin
GAPDH
B
Top enriched KEGG pathwayhs in THBS1-2h vs THBS1-0h
Proteoglycans in cancer
Adherens junction
Epithelial cell signaling
Bacterial invasion of epithelial cells
PI3K−AKT signaling pathway
Spliceosome
ECM−receptor interaction
Focal adhesion
Relaxin signaling pathway
Hepatitis C
Hippo signaling pathway
0
1
2
−Log10 Fisher's exact test p value
C
Shared phosphopeptides
all conditions
shared in PI3K-AKT
shared in fiber
shared in mesenchymal
Pathway
Fiber- related
Mesenchymal
PI3K-AKT
Condition
THBS1-0h
THBS1-2h
THBS1-12h
THBS1-12h
THBS1-0h
THBS1-2h
PML S480
PAFAH1B2 S6
AHNAK S5110
AHNAK S3426
AHNAK S5099
ADD1 S436
SHROOM3 S242
RB1 T823
SLC9A1 S796
SLC9A1 S703
EGFR Y1197
GNG12 S49
AKT1 S122
HSP90AA1 T594
BAD Y76
MFAP1 S132
MFAP1 S133
KRT8 S253
FLNC S2598
CAV2 S36
ACTB S234
ADD1 S64
RTN4 S12
MAP1S S762
DBN1 S142
RAI14 T295
ERBB2 S1054
BRCA1 S1342
TCOF1 S679
KRT19 Y391
CDK5RAP2 S1350
SLAIN2 S315
SLAIN2 S147
SLAIN2 S435
PKP2 S172
D
Co-culture with BMDM
BR NC
24h
48h
p-DBN1
DBN1
Vimentin
GAPDH
E
NC
Co-culture with BMDM
HGDMEM
Rapamycin
HuCCT1
BR
F
NC
Rapamycin
THBS1
Rapamycin +THBS1
HuCCT1
BR
G
(i) NC
BTP2
5 μM
25 μM
125 μM
HuCCT1
(ii) NC
BTP2
25 μM
125 μM
BR
H
HuCCT1
NC BTP2
p-DBN1
DBN1
p-mTORC1
Vimentin
CD47
GAPDH
I
Thbs1fl/fl
Thbs1fl/fl ;Lyz-Cre
Hydrodynamic injection of AKT1/NICD1
Sacrifice mice 4 weeks post-injection or moribund
J
AKT1/NICD1
Hepatosomatic index
0.4
0.3
0.2
0.1
0.0
*
Thbs1fl/fl
Thbs1fl/fl ;Lyz-Cre
K
Thbs1fl/fl AKT1/NICD1
Thbs1fl/fl ;Lyz-Cre AKT1/NICD1
L
Thbs1fl/fl
Thbs1fl/fl; Lyz-Cre
AN-1
AN-2
AN-3
AN-4
AN-1
AN-2
AN-3
AN-4
THBS1
CD47
DBN1
p-DBN1
p-mTOR1
Vimentin
GAPDH
β-Actin

682 **Fig. 6.**

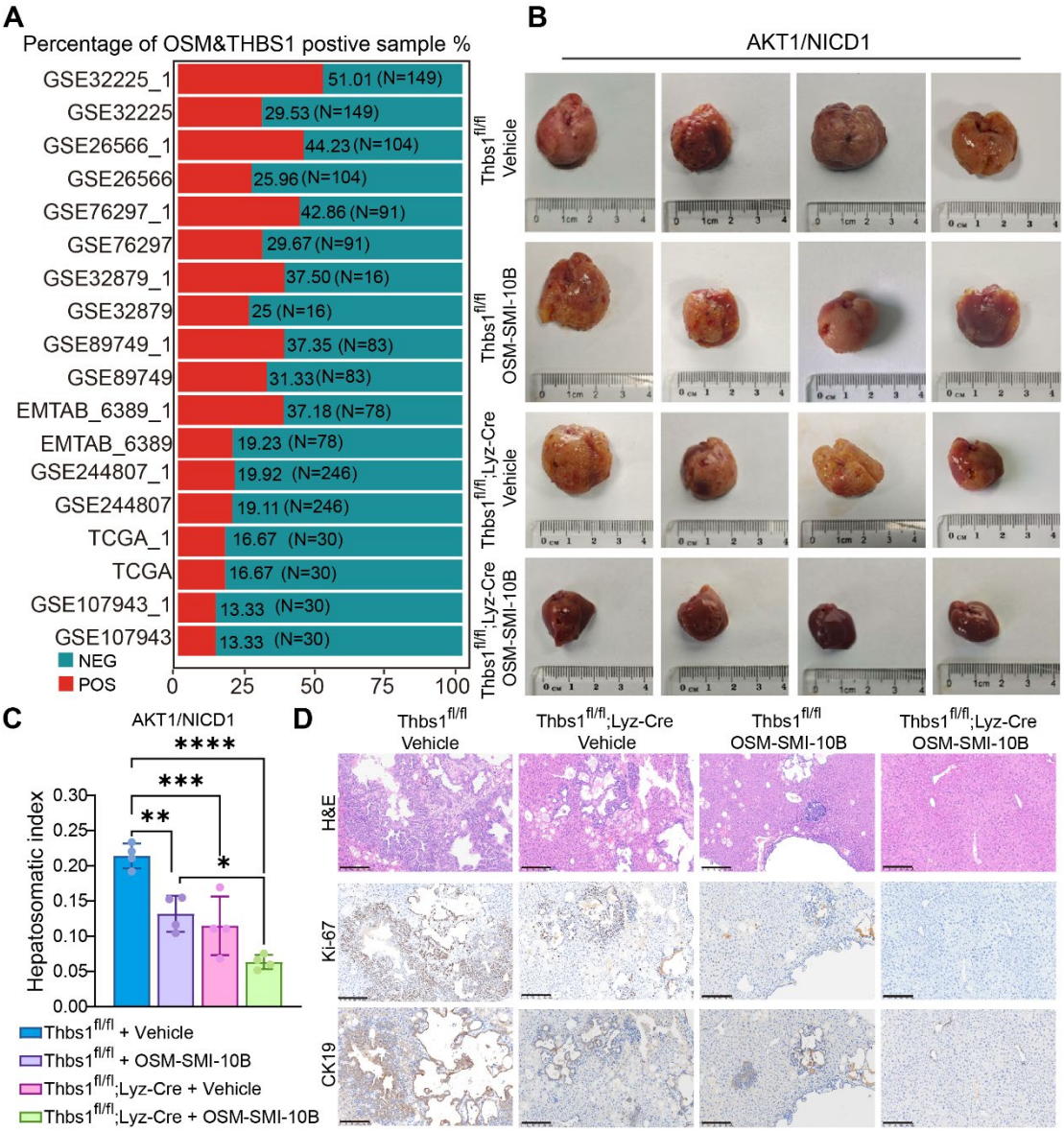

683

684

Fig. 7.

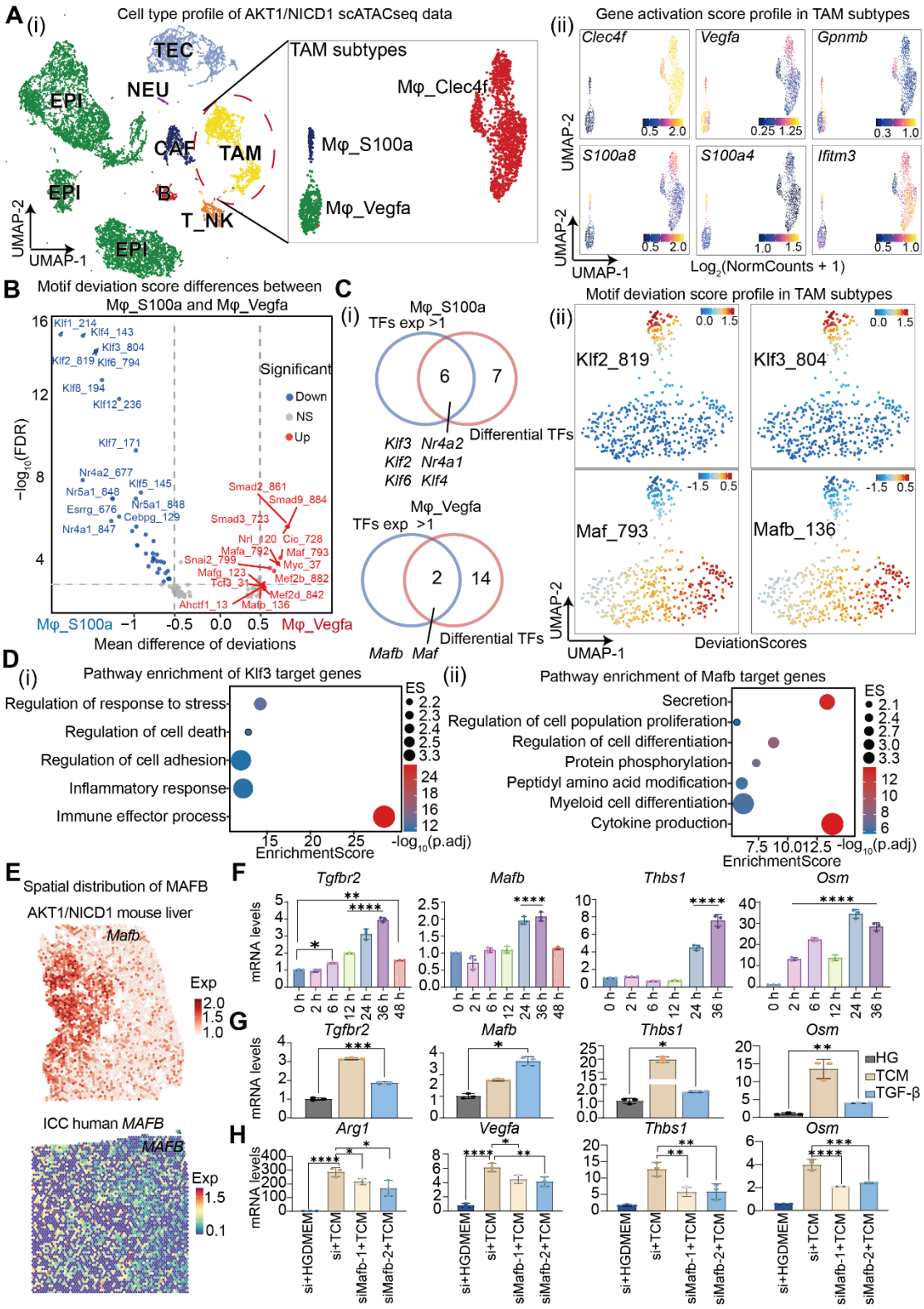
A (i)
Cell type profile of AKT1/NICD1 scATACseq data
TEC
NEU
EPI
CAF
TAM
B
T_NK
TAM subtypes
Mφ_Clec4f
Mφ_S100a
Mφ_Vegfa
UMAP-2
UMAP-1
(ii)
Gene activation score profile in TAM subtypes
Clec4f
Vegfa
Gpnmb
S100a8
S100a4
Ifitm3
Log2(NormCounts + 1)
B
Motif deviation score differences between Mφ_S100a and Mφ_Vegfa
Significant
Down
NS
Up
−log10(FDR)
Mφ_S100a
Mφ_Vegfa
Mean difference of deviations
C
(i)
Mφ_S100a
TFs exp >1
Differential TFs
Klf3 Nr4a2
Klf2 Nr4a1
Klf6 Klf4
Mφ_Vegfa
TFs exp >1
Mafb Maf
(ii)
Motif deviation score profile in TAM subtypes
Klf2_819
Klf3_804
Maf_793
Mafb_136
DeviationScores
D
(i)
Pathway enrichment of Klf3 target genes
Regulation of response to stress
Regulation of cell death
Regulation of cell adhesion
Inflammatory response
Immune effector process
ES
EnrichmentScore
-log10(p.adj)
(ii)
Pathway enrichment of Mafb target genes
Secretion
Regulation of cell population proliferation
Regulation of cell differentiation
Protein phosphorylation
Peptidyl amino acid modification
Myeloid cell differentiation
Cytokine production
E
Spatial distribution of MAFB
AKT1/NICD1 mouse liver
Mafb
Exp
ICC human MAFB
MAFB
F
Tgfbr2
Mafb
Thbs1
Osm
mRNA levels
G
HG
TCM
TGF-β
H
Arg1
Vegfa
si+HGDMEM
si+TCM
siMafb-1+TCM
siMafb-2+TCM